

Research Article

Optical and Magnetic Properties of Ni Doped ZnS Diluted Magnetic Semiconductors Synthesized by Hydrothermal Method

Meirong Wu,^{1,2} Zhiqiang Wei,^{1,2} Wenhua Zhao,¹ Xuan Wang,² and Jinlong Jiang²

¹State Key Laboratory of Advanced Processing and Recycling Nonferrous Metals, Lanzhou University of Technology, Lanzhou 730050, China

²School of Science, Lanzhou University of Technology, Lanzhou 730050, China

Correspondence should be addressed to Zhiqiang Wei; qianweizuo@163.com

Received 24 March 2017; Revised 16 June 2017; Accepted 12 July 2017; Published 11 September 2017

Academic Editor: Marinella Striccoli

Copyright © 2017 Meirong Wu et al. This is an open access article distributed under the Creative Commons Attribution License, which permits unrestricted use, distribution, and reproduction in any medium, provided the original work is properly cited.

Diluted magnetic semiconductors $Zn_{1-x}Ni_xS$ with different consistency ratio ($x = 0, 0.01, 0.03, 0.05, \text{ and } 0.07$) were successfully synthesized by hydrothermal method using ethylenediamine as a modifier. The influence of Ni doping concentration on the microstructure, morphology, and optical and magnetic properties of undoped and Ni doped ZnS nanocrystals was characterized by X-ray diffraction (XRD), high-resolution transmission electron microscopy (HRTEM), X-ray energy dispersive spectrometry (XEDS), ultraviolet-visible spectroscopy (UV-vis), Fourier transform infrared spectroscopy (FT-IR), photoluminescence spectra (PL), and the vibrating sample magnetometer (VSM), respectively. The experiment results show the substitution of Ni^{2+} on Zn^{2+} sites without changing the hexagonal wurtzite structure of ZnS and generate single-phase $Zn_{1-x}Ni_xS$ with good crystallization. The lattice constant causes distortion and decreases with the increase of Ni^{2+} doped concentration. The appearance of the samples is one-dimensional well-dispersed nanorods. UV-vis spectra reveal the band gap of all $Zn_{1-x}Ni_xS$ samples greater than that of bulk ZnS (3.67 eV), and blue shift phenomenon occurs. The photoluminescence spectra of undoped and doped samples possess the broad blue emission band in the range of 400–650 nm; the PL intensities of $Zn_{1-x}Ni_xS$ nanorods increase with the increase of Ni content comparing to pure ZnS and reach maximum for $x = 0.03$. Magnetic measurements indicated that the undoped ZnS samples are superparamagnetic, whereas the doped samples exhibit ferromagnetism.

1. Introduction

Diluted magnetic semiconductors refer to a new type of semiconductor material with both spin and charge degrees of freedom that is formed by the substitution of transition metals and rare earth ions to a small fraction of nonmagnetic cations in nonmagnetic semiconductors [1, 2]. DMS nanocrystals have attracted scientific community for new spintronic optoelectronic devices due to its novel properties and broad application prospect, such as field-emission devices, spin field-effect transistors, spin polarized light emitting diode, optical isolator, and quantum computer [3–8].

ZnS is one of the prospective candidates for multifunctional semiconductor material device because of its wide band gap (3.67 eV), free exciting binding energy (60 meV), and high index of refraction (2.27) and it possesses good

piezoelectric, ferromagnetic, photoelectric, and photosensitive properties. In addition, ZnS nanocrystals also have high specific surface area and quantum size effect and quantum tunneling effect [9–11], leading to the zinc sulfide doped matrix material exhibiting high quantum efficiency in photoluminescence and electroluminescence, and are often used as an important matrix material multicolor fluorescent powder. Therefore, in order to obtain the intrinsic dilute magnetic semiconductors, transition metal doped ZnS has been widely studied by different methods. The carrier type, sulfur vacancy, zinc interstitial defect, and crystallization quality of ZnS can be adjusted by changing the doping elements type and doping amount, controlling the preparation process, so as to effectively control the electrical, magnetic, and optical properties of ZnS [12–16]. Compared with the traditional ways, it can produce many kinds of nanometer powder by hydrothermal method. And its products have high purity,

small size, uniform distribution, and well chemical activity at low temperature. The solvent interact with the reactants at the molecular level, which provides a better control of stoichiometry, easy control of composition and structure, and ability to tailor particle size and morphology [17, 18]. At present, the scientific research on the microstructure and optical and magnetic properties of Ni doped ZnS is not systematic and comprehensive.

In this paper, we successfully synthesized the $Zn_{1-x}Ni_xS$ diluted magnetic semiconductors with different doping consistency ($x = 0, 0.01, 0.03, 0.05, \text{ and } 0.07$) by hydrothermal method. Using the testing method of HRTEM, XRD, XEDS, UV-vis, FT-IR, PL, and VSM, the sample's properties and microstructure were identified, including structure, morphology, constituent elements, and optical and magnetic properties.

2. Experimental

$Zn_{1-x}Ni_xS$ ($x = 0, 0.01, 0.03, 0.05, \text{ and } 0.07$) nanocrystals were prepared using hydrothermal method. All chemical products used in this study are analytical grade and used without further purification. The manufacturing process is as follows: according to the chemical formula $Zn_{1-x}Ni_xS$ and the mole ratio of the metal cation, weighed stoichiometric $Zn(Ac)_2 \cdot 2H_2O$, $(NH_2)_2CS$, and $Ni(Cl)_2 \cdot 6H_2O$ were dissolved in 80 ml ethylenediamine ($C_2H_8N_2$) and deionized water (1:1 in volume ratio) to obtain a solution; the solution was stirred until completely dissolved by magnetic stirrer at room temperature for 1 hour. And then the resulting mixed solution was transferred into a 100 ml Teflon-lined stainless steel autoclave (with the filling ratio of 80%), sealed, and maintained at $200^\circ C$ for 12 h in an oven. After the end of the reaction, the autoclave was taken out and cooled down to room temperature naturally. Finally, the resulting precipitate was repeated alternately washed with deionized water and absolute alcohol several times by centrifugation to remove impurities. The obtained products were dried in oven at $60^\circ C$ for 10 h. Thus, $Zn_{1-x}Ni_xS$ nanocrystals were collected and used for further studies.

The phase and crystalline structures of $Zn_{1-x}Ni_xS$ nanorods were investigated by a Japan Rigaku D/Max-2400 powder X-ray diffractometer with Cu-K α ($\lambda = 1.54056 \text{ \AA}$) radiation. The size and morphology of the samples were observed using high-resolution transmission electron microscopy (HRTEM, JEM-2010) coupled with an X-ray energy dispersive spectroscopy (XEDS) accessory to the chemical composition of the products. The absorption spectra of samples were recorded using ultraviolet-visible (UV-VIS, TU-1901) spectrophotometer. Fourier transform infrared spectroscopy (FT-IR) studies were carried out on Nexus 670 FT-IR spectrometer. Photoluminescence (PL) spectra measurements were performed on a PerkinElmer fluorescence spectrometer by using He-Cd laser as the excitation source with the excitation wavelength of 325 nm. Magnetic hysteresis loops were made at room temperature using a vibrating sample magnetometer (VSM, Lakeshore 7304) with the maximum field of 8 kOe.

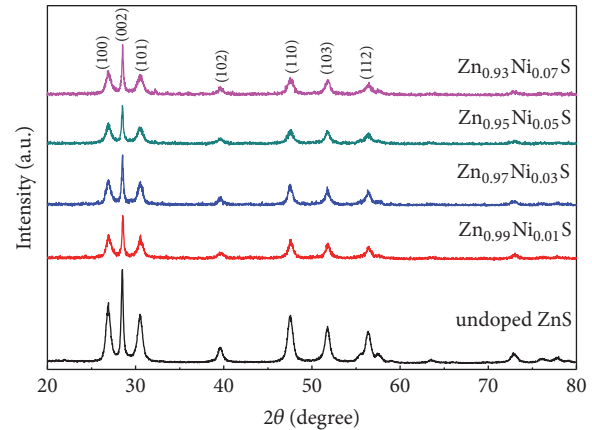


FIGURE 1: XRD patterns of $Zn_{1-x}Ni_xS$ ($x = 0, 0.01, 0.03, 0.05, \text{ and } 0.07$) nanorods.

3. Results and Discussion

3.1. Structural Analysis. To examine the crystalline structures and phase of the synthesized $Zn_{1-x}Ni_xS$ ($x = 0, 0.01, 0.03, 0.05, \text{ and } 0.07$) samples with different doping concentration ratio, XRD studies were carried out and the results are shown in Figure 1. It can be clearly observed from the pattern that the diffraction peaks located at $2\theta = 26.91^\circ, 28.50^\circ, 30.53^\circ, 39.61^\circ, 47.56^\circ, 51.78^\circ, \text{ and } 56.39^\circ$ corresponding to (100), (002), (101), (102), (110), (103), and (112) crystallographic planes of ZnS, respectively. All diffraction peaks can be well indexed as the hexagonal wurtzite phase ZnS crystalline structure, which are consistent with the standard spectrum (JCPDS number 36-1450). No diffraction peak of Ni and other impurity phases can be found in XRD diagram, confirming that there are no secondary phases such as metal clusters or metal oxides in the sample, indicating the formation of the pure single wurtzite phase ZnS when the doping atomic percentage ranges from 0% to 7%. Compared with the pure ZnS sample, the XRD intensity of the doped samples decreases, which may be attributed to declining the crystallization with Ni ion doping. Thus, it indicates that the change of molar ratio of doped elements does not cause the change of crystal structure of ZnS; Ni^{2+} is effectively introduced into the ZnS crystal lattice and substitutes for the Zn^{2+} site.

Based on the XRD results, the average crystalline size of $Zn_{1-x}Ni_xS$ samples can be estimated by using Scherrer formula:

$$D = \frac{K\lambda}{B \cos \theta}, \quad (1)$$

where D represents the average diameter, $K = 0.89$ is the Scherrer constant, $\lambda = 1.54056 \text{ \AA}$ is X-ray wavelength of Cu-K α radiation, θ is the diffraction angle for the (002) planes, and B is full width half maximum (FWHM) of (002) diffraction peak in radian. It is noticed that the (002) diffraction peak is much stronger and narrower than the other peaks and the (002) have a rapid growth as compared to (100) and (001), which demonstrates a preferential growth direction along the c -axis of the hexagonal crystal. In addition, the (002)

TABLE 1: Parameters of the XRD patterns for $Zn_{1-x}Ni_xS$ ($x = 0, 0.01, 0.03, 0.05, \text{ and } 0.07$) nanorods.

Ni concentration	2θ ($^\circ$)	d_{hkl} (\AA)	FWHM ($^\circ$)	Lattice constants (\AA)	D (nm)
0%	28.40	3.139	0.227	$a = 3.829, c = 6.279$	35
1%	28.49	3.130	0.258	$a = 3.824, c = 6.261$	33
3%	28.52	3.128	0.260	$a = 3.815, c = 6.255$	31
5%	28.62	3.117	0.263	$a = 3.805, c = 6.230$	30
7%	28.84	3.093	0.277	$a = 3.777, c = 6.190$	29

diffraction peak FWHM of Ni doped ZnS is greater than that of undoped samples, which further confirms Ni is entering the ZnS lattice and substitutionally replacing Zn ions in the lattice of the host material.

The corresponding parameters of $Zn_{1-x}Ni_xS$ samples calculated along (002) plane are shown in Table 1. The microstructure data of ZnS nanocrystals were estimated according to the Bragg formula:

$$2d_{hkl} \sin \theta = \lambda, \quad (2)$$

where d_{hkl} denotes the interplanar spacing corresponding to (hkl) crystalline plane and θ is Bragg's diffraction angle. The lattice parameters a and c can be calculated with the help of crystallographic formula:

$$a = d_{hkl} \sqrt{\frac{4}{3} (h^2 + hk + l^2) + \left(\frac{a}{c}\right)^2 l^2}. \quad (3)$$

The calculation results are given in Table 1. From Table 1, it can be found that the diffraction peaks position of (002) crystal plane for $Zn_{1-x}Ni_xS$ samples slightly shifts to higher diffraction angles, while the crystalline plane distance decreases with the increase of Ni doped content. It can be understood that the decrease of the crystalline plane distance will result in the increase of the diffraction angle. The lattice parameters a -axis and c -axis of Ni doped ZnS samples decrease with the increase of Ni^{2+} doped content, which can be attributed to the substitution of smaller ionic radii Ni^{2+} (0.68 \AA) into larger ionic radii Zn^{2+} (0.74 \AA) in the wurtzite structure and causing lattice distortion. Therefore, the crystalline size and the lattice parameter of the samples can be controlled by adjusting the ratio of the doped Ni, and the microstructure of the sample is changed.

3.2. Morphological Studies. In order to explore the surface morphology and microstructure of the obtained samples, the HRTEM observations of undoped and Ni doped ZnS samples were carried out. Figure 2 shows that all the samples are comprised of one-dimensional well dispersed rod-like structure with clear edge, smooth surface, and good length to diameter ratio. Figure 2(a) shows the typical HRTEM image of undoped ZnS sample, which possesses relatively uniform one-dimensional rod-like shape with average diameter around 10 nm, and the length of nanorods ranges from 100 to 150 nm. Compared with the pure ZnS nanorods, the $Zn_{0.97}Ni_{0.03}S$ nanorods have slight change in diameter and length shown in Figure 2(b), the diameter of Ni doped ZnS

sample is about 15 nm, and the length ranges from 50 to 100 nm. From the above observations, it can be noticed that the morphology of $Zn_{0.97}Ni_{0.03}S$ nanorods becomes shorter and coarser and the rod length diameter ratio becomes lower as compared to the undoped ZnS samples.

Figure 2(c) displays the local high magnification HRTEM micrographs of $Zn_{0.97}Ni_{0.03}S$ nanorods. It can be seen that the $Zn_{0.97}Ni_{0.03}S$ nanorods reveal the clear lattice fringe and no obvious defects and exhibit a well oriented growth along the (002) direction with good crystallization, The fringe spacing is about 0.311 nm, which is close to the interplanar distance of the (002) lattice planes of the standard wurtzite-type ZnS structure ($2\theta = 28.500, d = 0.313$ nm). However, the value of d spacing is smaller than bulk ZnS, which is due to the substitution of smaller ionic radii Ni^{2+} (0.68 \AA) into larger ionic radii Zn^{2+} (0.74 \AA). The TEM results are coincided with the conclusion obtained from XRD analysis, which further proved the substitution of Zn ions by Ni ions in the ZnS matrix. The corresponding selected area electron diffraction (SAED) patterns of $Zn_{0.97}Ni_{0.03}S$ nanorods are shown in Figure 2(d). It can be found that the SAED pattern consists of many regular concentric rings with different radius, which indicate that the samples belong to polycrystalline structure. The diffraction ring from inside to outside is corresponding to (100), (002), (101), (102), (110), (103), and (112) planes of $Zn_{0.97}Ni_{0.03}S$ nanorods, respectively. The SAED pattern further confirms that the obtained samples belong to wurtzite structure and agreement with the result of XRD, indicating that the entry of Ni^{2+} ions does not degrade the crystallinity of samples.

3.3. Chemical Component Analysis. In order to determine the composition of the samples, the energy dispersive X-ray energy dispersive spectrometry (XEDS) of $Zn_{1-x}Ni_xS$ nanorods was performed. Figure 3 shows the XEDS patterns of the pure ZnS and $Zn_{0.97}Ni_{0.03}S$ nanorods. The XEDS spectra of the pure sample are present in Figure 3(a); in addition to the existence of the characteristic peaks of Zn and S element, it contains C, O, and Cu element. The C and O elements may be introduced in the process of washing the samples, which cannot be completely washed with distilled water and absolute alcohol. The Cu peaks are attributed to the micro grid of the bearing samples during the testing process. The XEDS spectra analysis of $Zn_{0.97}Ni_{0.03}S$ nanorods in Figure 3(b) confirms the presence of Ni elements in samples. The quantitative atomic and weight percentage of the compositional elements are given in the inset of Figure 3.

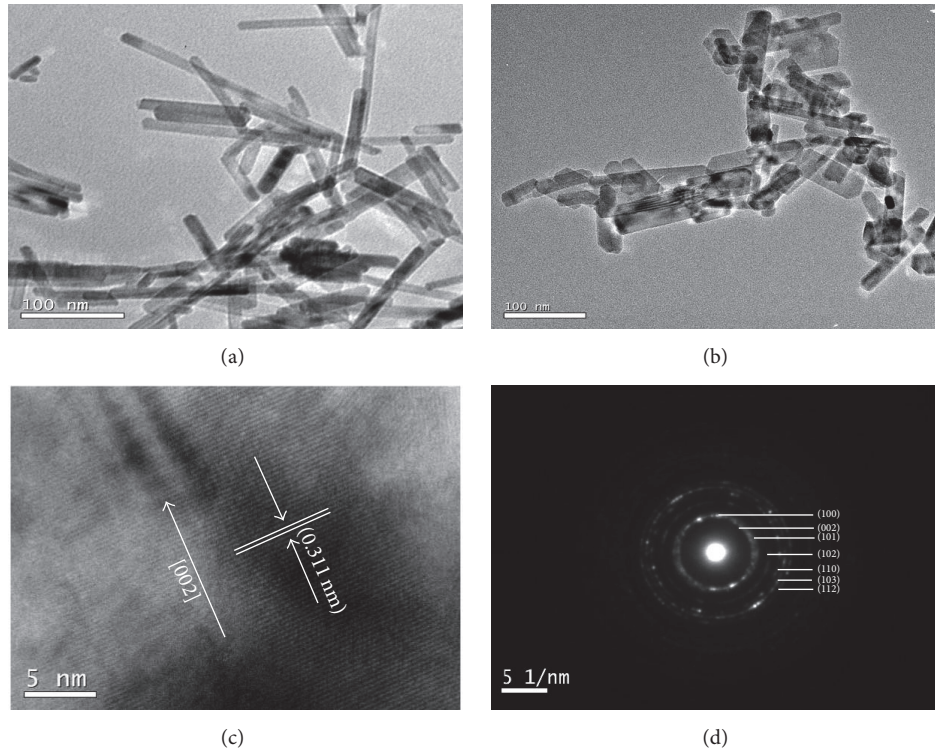


FIGURE 2: HRTEM images (a–c) and SAED (d) pattern of ZnS and Zn_{0.97}Ni_{0.03}S nanorods.

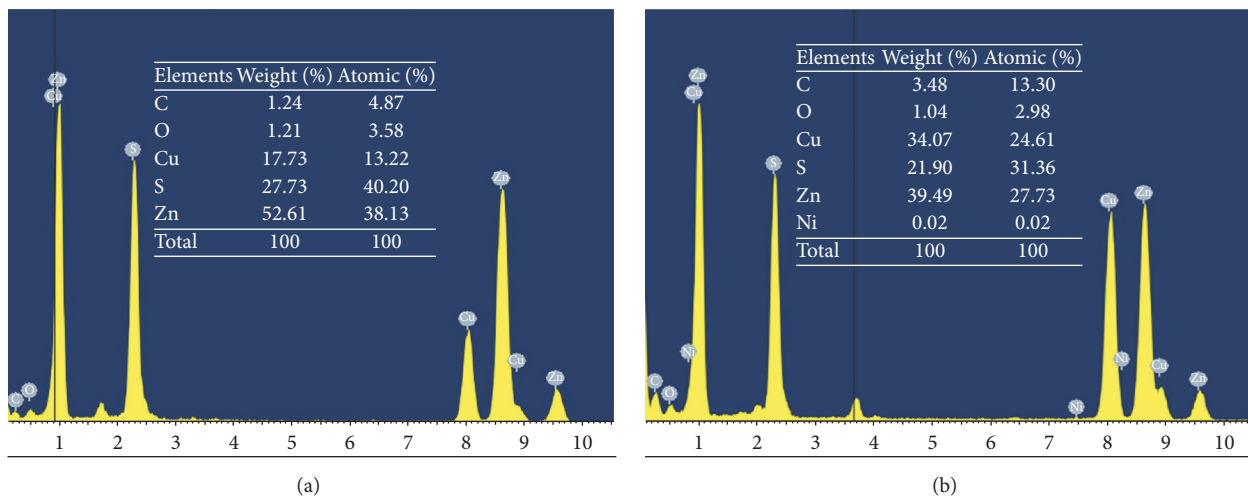


FIGURE 3: XEDS patterns of pure ZnS and Zn_{0.97}Ni_{0.03}S nanorods.

It can be found the calculated weight and atomic percentage are close to the nominal stoichiometry within the experimental error. The XEDS results further verify XRD conclusion, which indicates that Ni is entering the ZnS diluted magnetic semiconductor and replacing Zn ions in ZnS matrix.

3.4. FT-IR Analysis. In order to investigate the effect of Ni doping on the optical characteristics of Zn_{1-x}Ni_xS samples, the optical absorption spectra were analyzed using FT-IR spectrometer. Figure 4 shows the FT-IR analysis of Zn_{1-x}Ni_xS

($x = 0, 0.01, 0.03, 0.05, \text{ and } 0.07$) samples in the range of 500–4000 cm^{-1} . For all the samples, the broad peak centered at about 3433 cm^{-1} can be assigned to the longitudinal stretching vibration mode of chemically bonded hydroxyl groups, resulting from small quantity of adsorbed H₂O on the sample. The weak bands at 2941 and 2857 cm^{-1} are attributed to the N-H stretching vibration of ethylenediamine. The band at 1635 cm^{-1} corresponds to the deformation vibration of water molecule. The band at 1005 to 1280 cm^{-1} weak vibration modes may be assigned to the organic compounds, which

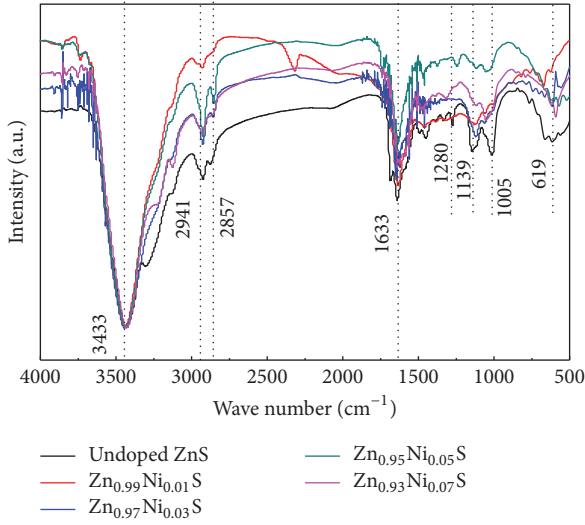


FIGURE 4: FT-IR spectra of $\text{Zn}_{1-x}\text{Ni}_x\text{S}$ ($x = 0, 0.01, 0.03, 0.05,$ and 0.07) nanorods.

may come from the ethylenediamine or alcohol used in the process of preparation [19]. In addition, the wurtzite structure can be identified by the peak at 669 cm^{-1} , assigned to a Zn–S bond. With the increasing Ni^{2+} concentration, the FT-IR spectra of all the samples were not changed obviously, which proved that Ni^{2+} successfully substituted for the lattice site of Zn^{2+} and into the ZnS host lattice without altering the crystal structure. This result is in good agreement with the XRD result.

3.5. UV-Visible Studies. The UV-vis optical absorption spectra for $\text{Zn}_{1-x}\text{Ni}_x\text{S}$ ($x = 0, 0.01, 0.03, 0.05,$ and 0.07) samples were recorded at room temperature in the wavelength range of 250–700 nm; as shown in Figure 5, it is clear that all $\text{Zn}_{1-x}\text{Ni}_x\text{S}$ samples exhibit strong absorption edges band at UV region in the range of 260–300 nm and poor absorption at visible region. The gradual doping substitution of Ni^{2+} in ZnS lattice results in the difference of absorption coefficient of sample and also has some influence on the position of absorption peak.

Based on the UV-vis results, the optical band gap can be calculated according to Tauc relation as follows:

$$\alpha h\nu = A(h\nu - E_g)^n, \quad (4)$$

where A is a constant, h is Plank's constant, $h\nu$ is the incident photon energy, E_g is the band gap of samples, and α is the absorption coefficient which can be obtained using the Kubelka–Munk function:

$$\alpha = F(R) = \frac{(1-R)^2}{2R}, \quad (5)$$

where R is the percentage of reflected light. For ZnS nanocrystals semiconductor with direct band structure, $n = 1/2$ and $(\alpha h\nu)^2$ gives the best linear fitting curve in the band edge region. The relationship between $(\alpha h\nu)^2$ and $h\nu$ is shown

in Figure 5(b). The values of E_g are obtained by extrapolating the straight portion of the curve on $h\nu$ axis at $\alpha = 0$. The measured values of optical band gap energy for $\text{Zn}_{1-x}\text{Ni}_x\text{S}$ ($x = 0, 0.01, 0.03, 0.05,$ and 0.07) nanorods are 3.79, 3.77, 3.74, 3.75, and 3.76 eV, respectively. It was clearly that the direct band gap values of all $\text{Zn}_{1-x}\text{Ni}_x\text{S}$ samples are greater than that of bulk ZnS (3.67 eV), and blue shift phenomenon occurs. The blue shift phenomenon is caused by the quantum size effect changes of the electronic transition; due to the decrease of the nanoparticle size, the energy gap becomes wider, which leads to the optical absorption band shift to the short wave direction. On the other hand, small particle size and large surface tension lead to distortion of lattice, the lattice constants decrease, the distortion inside the particle makes the bond length shorter, and the infrared absorption band shifts to higher wave number; the interface effect caused spectral blue shift of nanomaterials.

Furthermore, the influences of Ni doping concentration on the band gap energy of $\text{Zn}_{1-x}\text{Ni}_x\text{S}$ samples are indicated in the inset of Figure 5(b). It is worth noting that the band gap of Ni doped ZnS samples is lower than that of undoped sample and the value gradually decreases with the increase of Ni doped concentration and the band gap up to a minimum 3.74 eV for 3% Ni, whereas when the Ni doping concentration is greater than 3%, the band gap of $\text{Zn}_{1-x}\text{Ni}_x\text{S}$ samples increases slightly with the increase of Ni concentration. The observed lower band gap (red shift) at low doping concentration may be due to the sp-d spin exchange interactions. The correction probability of the positive and negative potential to the conduction band and the valence band edge may be enhanced, respectively, under the s-d and p-d exchange interactions, which result in band gap narrowing [20]. But the higher band gap (blue shift) at high doping (from 3% to 7% Ni) may be explained by the Burstein–Moss shift; when the doping concentration of Ni ion is rather high, the carrier density donated by Ni ions will increase [21]. The increase of carrier density shifts the Fermi level close to conduction band and the changes of transition levels lead to the energy gap broadening.

3.6. Photoluminescence Studies. The most effective tool for exploring the defect structure in semiconductor is nondestructive photoluminescence (PL) measurements. It helps to characterize the impurity and defect energy states even when they are presented in very low concentrations whether at surface or interfaces. Figure 6(a) shows the room photoluminescence spectra of $\text{Zn}_{1-x}\text{Ni}_x\text{S}$ samples. It exhibits that all samples possess the broad blue emission band in the range of 400–650 nm, and the broad emission bands may be attributed to the recombination of electron hole induced by the change of local charge distribution at the defect sites [22].

The PL emission intensity of $\text{Zn}_{1-x}\text{Ni}_x\text{S}$ nanorods is indicated in the inset of Figure 6(a). It is noted that the PL intensities of $\text{Zn}_{1-x}\text{Ni}_x\text{S}$ nanorods exhibit dramatic change with the increase of doping amount; the PL emission intensity of the doped samples increases comparing to pure ZnS. When Ni doping concentration $x = 0.03$, the intensity of the PL spectrum reaches maximum, whereas when the Ni doping concentration is greater than 3%, the intensity of $\text{Zn}_{1-x}\text{Ni}_x\text{S}$

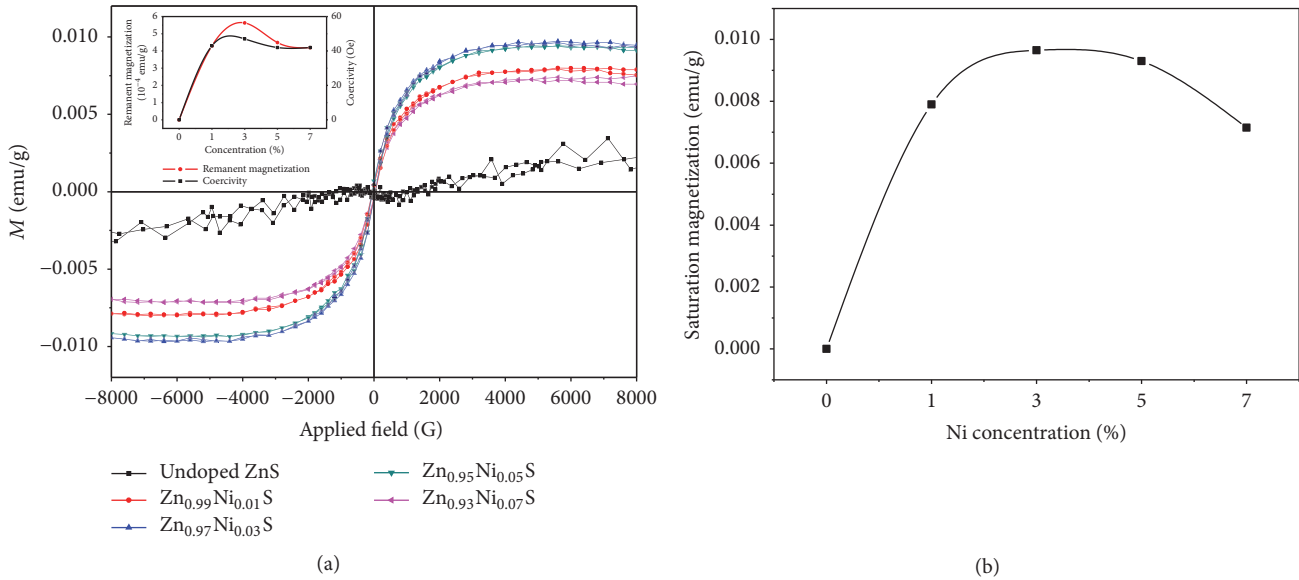


FIGURE 7: (a) Room temperature M-H plots of $Zn_{1-x}Ni_x$ nanorods; (b) the variation of saturation magnetization with Ni doping concentration.

samples decreases slightly with the increase of Ni amount. The substitution of Zn^{2+} ions by Ni^{2+} ions could increase the number of trapped electron hole pairs and emit more photons and generate new radiation centers, which enhances the PL intensity [23]. The subsequent quenching may be attributed to the capture ability of transition metal nickel ions better than the anion vacancy defect centers to the photo-excited electrons. It has been reported that the doped transition metals act as electron trapping centers at higher doping concentration, which result in nonradiative recombination processes increase [24]. As a result, the continuous increase of Ni ion doping concentration will cause the quenching of PL emission intensity.

Pure ZnS samples show an asymmetric strong green emission peak at 510 nm, which can be decomposed into four Gaussian peaks, respectively, centered at 424 nm, 505 nm, 549 nm, and 628 nm as shown in Figure 6(b). According to the energy diagram of the defects distributed in the ZnS, generally speaking, the mechanism of PL emission in ZnS nanostructures is composed of two parts: the zinc vacancy (V_{Zn}) and the interstitial sulfur (I_S) atom as acceptor state and the sulfur vacancy (V_S) and interstitial zinc (I_{Zn}) atoms as the local donor state. Interstitial sulfur states should be located closer to the valence band edge than interstitial zinc states to the conduction band edge while sulfur vacancies should be located closer to the conduction band edge than zinc vacancies to the valence band edge. Moreover, energy levels of vacancies are deeper than interstitial states [25]. The violet emission band at 424 nm is a sulfur vacancy (V_S) assisted one, caused by the transition from the sulfur vacancy state to the valence band edge state of ZnS nanorods [26]. The emission band centered at 505 nm is attributed to the transfer of trapped electrons on sulfur vacancies to interstitial sulfur states producing the green luminescence. The emission band at 549 nm may be due to sulfur species on the surface of ZnS

NWs [27]. The orange emission peak at 628 nm is assigned to the recombination between the interstitial zinc states and the zinc vacancies [28]. Figure 6(c) shows the Gaussian fitting of PL data of $Zn_{0.97}Ni_{0.03}S$ nanorods; this spectrum consists of five emission bands centered at 436 nm, 492 nm, 520 nm, 543 nm, and 606 nm. In comparison with pure ZnS, an additional emission centered at around 520 nm is observed besides the emissions from pure ZnS. This emission is closely related to the ${}^3T_1-{}^3A_2$ transition within the 3F shell of Ni^{2+} ions; the lowest multiplet term 3F of the free Ni^{2+} ion is split into 3T_1 , 3T_2 , and 3A_2 by the anisotropic hybridization, resulting in the d-d photon transition in Ni^{2+} and forming the Ni^{2+} luminescence center in the ZnS [29]. And normally the observed green emission is related to the ${}^3T_1-{}^3A_2$ transition of Ni^{2+} ions. Thus, the emission centered at 520 nm in Figure 6(c) further validates that the Ni^{2+} ions successfully entered the ZnS host. Based on the above PL analysis, the schematic energy level mechanism of all these observed transitions above PL analysis in Ni doped ZnS nanostructures is shown in Figure 6(d).

3.7. Magnetic Properties. The magnetic behavior of Ni doped ZnS samples with different doping concentrations was measured at room temperatures by VSM using a magnetic field (H) of 8 kOe. The M-H curves of $Zn_{1-x}Ni_xS$ ($x = 0, 0.01, 0.03, 0.05, \text{ and } 0.07$) samples measured at room temperature are given in Figure 7(a). It shows that pure ZnS has paramagnetic behavior with few values of coercivity and remnant magnetization; whereas all Ni doped ZnS samples exhibited obvious ferromagnetic features at room temperature, the paramagnetic behavior of pure ZnS nanorods is ascribed to surface defects and is in corroboration with PL studies. Eryong et al. [30] have also observed such paramagnetic behavior in Fe-doped ZnS nanoparticles. The variation of coercivity

(Hc) and remanent magnetization (Ms) with Ni concentration of $Zn_{1-x}Ni_xS$ nanorods are indicated in the inset of Figure 7(a). Compared with paramagnetic behavior of pure ZnS, the origin of the observed ferromagnetic properties of Ni doped ZnS samples is mainly due to the substitution of Ni^{2+} on Zn^{2+} sites not due to Ni cluster or its metal oxides, proved by the XEDS and XRD studies; no such secondary phases have been observed.

The variation of saturation magnetization with Ni doping concentration of $Zn_{1-x}Ni_xS$ ($x = 0, 0.01, 0.03, 0.05, \text{ and } 0.07$) nanorods is given in Figure 7(b). The saturation magnetization of Ni doped samples is greater than that pure ZnS, which is due to very small size of Ni doped ZnS nanorods; surface to volume ratio is expected to be very high which further leads to surface defects [31, 32]. As the doping concentration of Ni ions increases the magnetization value also increases till reaching a maximum at 3%; subsequently, the saturation magnetization decreases with the increase of Ni concentration. There may be two exchange interactions in the presence of $Zn_{1-x}Ni_xS$ nanorods. On the one hand there is the nearest neighbor antiferromagnetic coupling of Ni ion pair in doped ZnS nanorods. On the other hand there is the exchange interaction between the localized “d” spin on Ni^{2+} and free delocalized carrier, which strongly depends on the hybridization between the d shell of Ni^{2+} ions and the p shell of their near neighbor S^{2-} ions [33]. When the doping concentration is low, the small magnetic dipoles existing on the surface of the nanorods interact with their nearest neighbors inside the particles, producing exchange energy that forces the other neighboring dipoles to be aligned in the same direction. Due to the high specific surface area of nanorods, the number of magnetic dipoles of the same orientation will be enhanced in the same direction [34, 35]. At the same time, the ferromagnetic coupling plays a dominant role in the ferromagnetic contribution to the sample. Consequently, the total magnetization increases with the Ni content till reaching a maximum at 3%. At higher dopant concentration, the Ni cation density increases with increased doping concentrations, which lead to the distance between Ni-Ni ions being decreased and antiferromagnetic interaction being strengthened. These antiferromagnetic coupling effects between Ni ions can quench the magnetic moment, resulting in lower total magnetization. The results indicate that for room temperature ferromagnetism enhancement of ZnS nanorods, the optimum doping level of Ni^{2+} is about 3%.

4. Conclusions

(1) Diluted magnetic semiconductors $Zn_{1-x}Ni_xS$ of the wurtzite structure with different consistency ratio ($x = 0, 0.01, 0.03, 0.05, \text{ and } 0.07$) were successfully synthesized via a hydrothermal method. All the samples synthesized by this method are one-dimensional rod-like shape with good dispersion; XRD studies exhibit the substitution of Ni^{2+} on Zn^{2+} sites without changing the hexagonal structure of ZnS and generate single-phase $Zn_{1-x}Ni_xS$.

(2) UV-vis spectra reveal the band gap of all $Zn_{1-x}Ni_xS$ samples greater than that of bulk ZnS (3.67 eV), and blue

shift phenomenon occurs. The photoluminescence spectra of doped and undoped samples possess the broad blue emission band in the range of 400–650 nm; the PL intensities of $Zn_{1-x}Ni_xS$ nanorods increase with the increase of Ni doping concentration comparing to pure ZnS and reach maximum for $x = 0.03$.

(3) Magnetic measurements indicate that the undoped ZnS samples are superparamagnetic, whereas the doped samples exhibit ferromagnetism. The saturation magnetization increase weakened significantly with increasing Ni concentration comparing to pure ZnS and reaches minimum for 3% Ni.

Conflicts of Interest

The authors declare that they have no conflicts of interest.

Acknowledgments

This work was supported by the National Natural Science Foundation of China (Grant no. 51261015) and the Natural Science Foundation of Gansu Province, China (Grant no. 1308RJZA238).

References

- [1] K. M. Yu, W. Walukiewicz, J. Wu, and et al., “Diluted II–VI oxide semiconductors with multiple band gaps,” *Physical Review Letters*, vol. 91, no. 24, Article ID 246403, pp. 246–403, 2003.
- [2] J. Tang and K. L. Wang, “Electrical spin injection and transport in semiconductor nanowires: challenges, progress and perspectives,” *Nanoscale*, vol. 7, no. 10, pp. 4325–4337, 2015.
- [3] P. Chuang, S.-C. Ho, L. W. Smith et al., “All-electric all-semiconductor spin field-effect transistors,” *Nature Nanotechnology*, vol. 10, no. 1, pp. 35–39, 2014.
- [4] H. Riel, L.-E. Wernersson, M. Hong, and J. A. Del Alamo, “III–V compound semiconductor transistors-From planar to nanowire structures,” *MRS Bulletin*, vol. 39, no. 8, pp. 668–677, 2014.
- [5] Y. Wang and N. Herron, “Nanometer-sized semiconductor clusters: materials synthesis, quantum size effects, and photophysical properties,” *The Journal of Physical Chemistry*, vol. 95, no. 2, pp. 525–532, 1991.
- [6] G. Miao and J. S. Moodera, “Spin manipulation with magnetic semiconductor barriers,” *Physical Chemistry Chemical Physics*, vol. 17, no. 2, pp. 751–761, 2015.
- [7] J. T. Muhonen, J. P. Dehollain, A. Laucht et al., “Storing quantum information for 30 seconds in a nanoelectronic device,” *Nature Nanotechnology*, vol. 9, no. 12, pp. 986–991, 2014.
- [8] M. J. Iqbal and S. Iqbal, “Synthesis of stable and highly luminescent beryllium and magnesium doped ZnS quantum dots suitable for design of photonic and sensor material,” *Journal of Luminescence*, vol. 134, pp. 739–746, 2013.
- [9] H. Kumar, P. B. Barman, and R. R. Singh, “Effect of size and shell: enhanced optical and surface properties of CdS, ZnS and CdS/ZnS quantum dots,” *Physica E: Low-Dimensional Systems and Nanostructures*, vol. 67, pp. 168–177, 2015.
- [10] Q.-L. Li and S.-N. Ding, “Multicolor electrochemiluminescence of core-shell CdSe@ZnS quantum dots based on the size effect,” *Science China Chemistry*, vol. 59, no. 11, pp. 1508–1512, 2016.

- [11] A. Fairbrother, V. Izquierdo-Roca, X. Fontané et al., "ZnS grain size effects on near-resonant Raman scattering: optical non-destructive grain size estimation," *Cryst Eng Comm*, vol. 16, no. 20, pp. 4120–4125, 2014.
- [12] D. A. Reddy, C. Liu, R. P. Vijayalakshmi, and B. K. Reddy, "Effect of Al doping on the structural, optical and photoluminescence properties of ZnS nanoparticles," *Journal of Alloys and Compounds*, vol. 582, pp. 257–264, 2014.
- [13] A. Roychowdhury, S. P. Pati, S. Kumar, and D. Das, "Effects of magnetite nanoparticles on optical properties of zinc sulfide in fluorescent-magnetic Fe₃O₄/ZnS nanocomposites," *Powder Technology*, vol. 254, pp. 583–590, 2014.
- [14] D. Saikia, R. Raland, and J. P. Borah, "Influence of Fe doping on the structural, optical and magnetic properties of ZnS diluted magnetic semiconductor," *Physica E: Low-Dimensional Systems and Nanostructures*, vol. 83, pp. 56–63, 2016.
- [15] J. Cao, D. Han, B. Wang et al., "Low temperature synthesis, photoluminescence, magnetic properties of the transition metal doped wurtzite ZnS nanowires," *Journal of Solid State Chemistry*, vol. 200, pp. 317–322, 2013.
- [16] A. Goktas, F. Aslan, and A. Tumbul, "Nanostructured Cu-doped ZnS polycrystalline thin films produced by a wet chemical route: the influences of Cu doping and film thickness on the structural, optical and electrical properties," *Journal of Sol-Gel Science and Technology*, vol. 75, no. 1, pp. 45–53, 2015.
- [17] K. Byrappa and T. Adschiri, "Hydrothermal technology for nanotechnology," *Progress in Crystal Growth and Characterization of Materials*, vol. 53, no. 2, pp. 117–166, 2007.
- [18] L. Wang, J. Dai, X. Liu, Z. Zhu, X. Huang, and P. Wu, "Morphology-controlling synthesis of ZnS through a hydrothermal/solvothermal method," *Ceramics International*, vol. 38, no. 3, pp. 1873–1878, 2012.
- [19] L. Chai, J. Du, S. Xiong, H. Li, Y. Zhu, and Y. Qian, "Synthesis of wurtzite ZnS nanowire bundles using a solvothermal technique," *Journal of Physical Chemistry C*, vol. 111, no. 34, pp. 12658–12662, 2007.
- [20] K. J. Kim and Y. R. Park, "Optical investigation of Zn_{1-x}Fe_xO films grown on Al₂O₃(0001) by radio-frequency sputtering," *Journal of Applied Physics*, vol. 96, no. 8, pp. 4150–4153, 2004.
- [21] M. F. Malek, M. H. Mamat, N. D. Md Sin, and M. Rusop, "Effects of Sn dopant on structural and optical properties of ZnO thin film prepared by sol-gel route," *Applied Mechanics and Materials*, vol. 773–774, pp. 617–621, 2015.
- [22] S. K. Mehta, S. Kumar, and M. Gradzielski, "Growth, stability, optical and photoluminescent properties of aqueous colloidal ZnS nanoparticles in relation to surfactant molecular structure," *Journal of Colloid and Interface Science*, vol. 360, no. 2, pp. 497–507, 2011.
- [23] N. Dixit, N. Anasane, M. Chavda, D. Bodas, and H. P. Soni, "Inducing multiple functionalities in ZnS nanoparticles by doping Ni₄₊₂ ions," *Materials Research Bulletin*, vol. 48, no. 6, pp. 2259–2267, 2013.
- [24] G. Rani and P. D. Sahare, "Spectroscopy of nickel-doped zinc sulfide nanoparticles," *Spectroscopy Letters*, vol. 46, no. 6, pp. 391–396, 2013.
- [25] H. Tang, G. Xu, L. Weng, L. Pan, and L. Wang, "Luminescence and photophysical properties of colloidal ZnS nanoparticles," *Acta Materialia*, vol. 52, no. 6, pp. 1489–1494, 2004.
- [26] V. P. Devarajan, D. Nataraj, T. Pazhanivel et al., "Molecular conformation dependent emission behaviour (blue, red and white light emissions) of all-trans- β -carotene-ZnS quantum dot hybrid nanostructures," *Journal of Materials Chemistry*, vol. 22, no. 35, pp. 18454–18462, 2012.
- [27] Z. Li, B. Liu, X. Li et al., "Synthesis of ZnS nanocrystals with controllable structure and morphology and their photoluminescence property," *Nanotechnology*, vol. 18, no. 25, Article ID 255602, 2007.
- [28] X. Wang, J. Shi, Z. Feng, M. Li, and C. Li, "Visible emission characteristics from different defects of ZnS nanocrystals," *Physical Chemistry Chemical Physics*, vol. 13, no. 10, pp. 4715–4723, 2011.
- [29] P. Yang, M. Lü, D. Xü et al., "Strong green luminescence of Ni₂₊-doped ZnS nanocrystals," *Applied Physics A: Materials Science & Processing*, vol. 74, no. 2, pp. 257–259, 2002.
- [30] N. Eryong, L. Donglai, Z. Yunsen et al., "Photoluminescence and magnetic properties of Fe-doped ZnS nano-particles synthesized by chemical co-precipitation," *Applied Surface Science*, vol. 257, no. 21, pp. 8762–8766, 2011.
- [31] P. Kaur, S. Kumar, C.-L. Chen et al., "Gd doping induced weak ferromagnetic ordering in ZnS nanoparticles synthesized by low temperature co-precipitation technique," *Materials Chemistry and Physics*, vol. 186, pp. 124–130, 2017.
- [32] P. Kaur, S. Kumar, A. Singh et al., "Investigations on doping induced changes in structural, electronic structure and magnetic behavior of spintronic Cr-ZnS nanoparticles," *Superlattices and Microstructures*, vol. 83, pp. 785–795, 2015.
- [33] P. K. Sharma, R. K. Dutta, and A. C. Pandey, "Effect of nickel doping concentration on structural and magnetic properties of ultrafine diluted magnetic semiconductor ZnO nanoparticles," *Journal of Magnetism and Magnetic Materials*, vol. 321, no. 20, pp. 3457–3461, 2009.
- [34] S. Kumar, C. L. Chen, C. L. Dong et al., "Room temperature ferromagnetism in Ni doped ZnS nanoparticles," *Journal of Alloys and Compounds*, vol. 554, pp. 357–362, 2013.
- [35] P. Kaur, S. Kumar, A. Singh, and S. M. Rao, "Improved magnetism in Cr doped ZnS nanoparticles with nitrogen co-doping synthesized using chemical co-precipitation technique," *Journal of Materials Science: Materials in Electronics*, vol. 26, no. 11, pp. 9158–9163, 2015.



Hindawi

Submit your manuscripts at
<https://www.hindawi.com>

